Small Structures

small structures

www.small-structures.com

RESEARCH ARTICLE OPEN ACCESS

Two-Dimensional Frameworks From Metal Oxo Clusters at Liquid Interfaces

Ajmal Roshan Unniram Parambil[1,2] | Muhammed Jibin Parammal[2] | Prashant Hitaishi[3,4] | Seyed Amirabbas Nazemi[1] | Narmadha Devi Suresh Kumar[5] | Alla Sologubenko[6] | Stephan Handschin[6] | Bridget M. Murphy[3,4] | Thomas A. Jung[5] | Jonathan De Roo[2] | Patrick Shahgaldian[1]

[1]Institute of Chemistry and BioanalyticsSchool of Life Sciences, University of Applied Sciences and Arts Northwestern Switzerland, Muttenz, Switzerland | [2]Department of Chemistry, University of Basel, Basel, Switzerland | [3]Institute of Experimental and Applied Physics, Kiel University, Kiel, Germany | [4]Ruprecht Haensel Laboratory, Kiel University, Kiel, Germany | [5]Laboratory for Micro- and Nanotechnology, Paul Scherrer Institute, Villigen, Switzerland | [6]Scientific Center for Light and Electron Microscopy (ScopeM), ETH Zürich, Zürich, Switzerland

Correspondence: Jonathan De Roo (jonathan.deroo@unibas.ch) | Patrick Shahgaldian (patrick.shahgaldian@fhnw.ch)

Received: 8 January 2026 | **Revised:** 5 February 2026 | **Accepted:** 10 February 2026

Keywords: Langmuir–Blodgett films | metal oxo cluster | metal–organic frameworks | pair distribution function | self-assembly

ABSTRACT

We report the realization of a two-dimensional analog of the archetypical metal-organic framework UiO-66 as a Langmuir monolayer, constructed from preformed metal oxo clusters and amphiphilic terephthalic acid ligands at the air–water interface. Structural changes of the metal oxo clusters in aqueous solution were elucidated to clarify their role in interfacial self-assembly at the water surface. Langmuir balance studies demonstrated that self-assembly with specifically designed organic linkers proceeds through a coordination-driven process. The resulting films were characterized by complementary techniques to determine their morphology, thickness, and composition. Based on these findings, a packing model of the monolayer was proposed. Finally, we extended this coordination-driven self-assembly strategy beyond aqueous systems to form, for the first time, monolayers at the air–*N*, *N*-dimethylformamide interface.

1 | Introduction

Efforts devoted by scientists in the late 20th century toward crystal engineering sparked the discovery of metal–organic frameworks (MOFs), an exceptional class of crystalline materials with unparalleled physical properties including high porosity and large surface area, as well as tunable architectures [1]. The accumulation of knowledge and a revival of interest among chemists in designing materials with meticulous control on their molecular architecture subsequently laid the foundation for reticular chemistry, enabling the systematic synthesis of a vast array of MOF structures. This breakthrough facilitated their rapid transition from the laboratory to the market, with several commercial products employing MOFs in applications ranging from gas storage to separation [2–4]. Nevertheless, their full potential remains constrained by technical bottlenecks primarily attributed to the poor utilization of metal sites, limited accessible surface area, and limited mass transport within MOFs [5, 6]. To tackle these challenges, MOFs can be size-tuned to 0D, 1D, or two-dimensional (2D) supramolecular architectures while maintaining crystallinity. Among them, 2D MOF nanosheets are an interesting class of materials due to their milder reaction conditions and more controllable synthesis approach, and properties that differ from bulk analogs [7]. 2D MOFs comprise a single layer or multiple layers of such hybrid nanosheets stacked in one direction. Such a layered structure enables 2D MOFs to enhance the accessibility of active metal sites, resulting in higher catalytic activity [8–10], improved porosity and specific surface area [11], and better electrical conductivity compared to their bulk analogs [12, 13].

The inorganic nodes of MOFs are typically constructed using mono- to tetravalent metal cations. Recently, there has been

significant interest in MOFs featuring tetravalent cations, particularly with group 4 metals (Zr^{4+}, Hf^{4+}) due to their remarkable chemical and hydrothermal stability, structural tunability, and biocompatibility [14–16]. Notable examples include UiO-66 and MOF-808; which are constructed from $Zr_6O_4(OH)_4$ secondary building units (SBUs), where an octahedral zirconium oxo cluster core is connected to polytopic benzene carboxylate linkers to generate rigid 3D structures [17, 18]. Group 4 metal oxo clusters are discrete molecular compounds [19]. The simplest example is a **Zr6** cluster capped with carboxylate ligands, $Zr_6O_4(OH)_4(OOCR)_{12}$ (Scheme 1A). The $Zr_6O_4(OH)_4^{12+}$ core consists of six zirconium and eight μ_3-oxygen atoms in an octahedral arrangement, stabilized by twelve surrounding carboxylate ligands. Notably, **Zr6** clusters can dimerize to form **Zr12** clusters if the capping carboxylate ligands lack branching at the α-carbon (Figure 1A) [20, 21]. Because of the lanthanide contraction, hafnium closely mimics zirconium in size and chemistry, giving rise to isostructural clusters and MOFs [19, 22]. Typically, MOFs are synthesized from metal precursors where metal oxo clusters form in situ before coordinating with organic ligands [23]. Lately, preformed metal oxo clusters have been used as SBUs in MOF synthesis to reach better morphological control and improved synthetic procedures [24]. Several Zr [15, 25–30], Hf [31, 32], and even mixed Zr-Hf [31] that could not be obtained through conventional solvothermal synthesis have been synthesized starting from metal oxo clusters as SBUs. Although all these syntheses involved either mechanochemical or solvo(hydro)thermal methods, starting from clusters does not necessarily require harsh reaction conditions such as high temperatures or toxic solvents like *N*, *N*-dimethylformamide (DMF). To date, most of the Zr/Hf-based 2D MOFs and metal–organic layers are synthesized from metal chlorides through bottom-up solvothermal synthesis [11, 33–41]. Top-down strategies for fabricating Hf-based 2D MOFs have also been explored [42]. Methods exploiting surfactant-mediated pseudoassembly to produce ultrathin 2D MOF nanosheets have also been reported, wherein the coordination ability of surfactants is utilized to weaken the interlayer interactions [43]. Zr oxo clusters have also been utilized as precursors for the seeded growth of UiO-66 membranes at room temperature [44]. However, despite the advances, metal oxo clusters have not been explicitly utilized as metal sources for synthesizing the highly desirable group 4 2D MOFs or metal–organic coordination networks (MOCNs).

One of the most widely used bottom-up approaches for synthesizing 2D MOFs and MOCNs is the interface-assisted method, where metal ions or clusters react with organic linkers at liquid–liquid, liquid–solid, or liquid–gas interfaces [45]. At the air–water interface, the Langmuir–Blodgett (LB) technique provides a confined 2D space for assembling ultrathin MOF nanosheets. The resulting layers can be transferred onto substrates for characterization and applications [46, 47]. The LB method has been used to produce several 2D MOFs or MOCNs, but mostly with metal ions rather than multinuclear clusters as inorganic nodes [48–51].

Herein, we report the first synthesis of a group 4 2D MOCN at the air–water interface, using tailor-made metal oxo cluster SBUs, achieved under mild, room temperature conditions. We target the 2D analog of UiO-66, where the well-known terephthalic acid links **Zr6** SBUs. To confine the growth of 2D MOCN at the surface, we designed a series of amphiphilic terephthalates with hydrophobic alkyl chains and hydrophilic carboxylate groups (Scheme 1B), which can readily form rigid monolayers at the surface of aqueous solutions containing low concentrations of clusters (Scheme 1C). The 2D MOCN monolayers were systematically investigated with the Langmuir balance method and Brewster angle microscopy (BAM). By combining findings from several techniques, including X-ray photoelectron spectroscopy (XPS), time-of-flight secondary ion mass spectrometry (ToF-SIMS), cryogenic scanning transmission electron microscopy (cryo-STEM), ellipsometry, atomic force

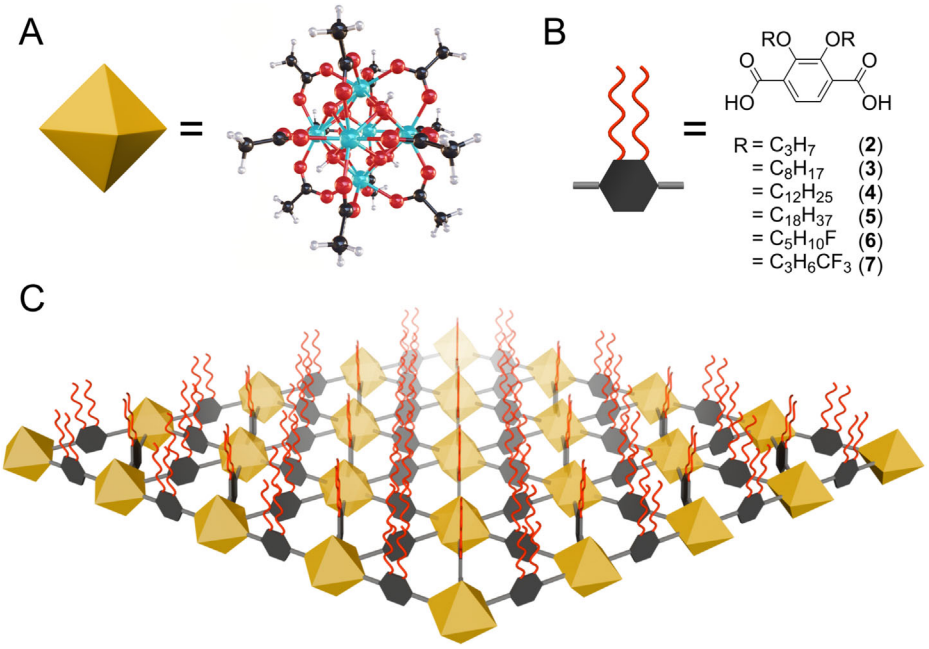

SCHEME 1 | (A) Structure of **M6**-acetate cluster ($M_6O_4(OH)_4(OOCR)_{12}$), where the $M_6O_8H_4$ core is capped with twelve acetate ligands, M = Zr/Hf. Cyan atoms represent zirconium or hafnium, all other atoms follow conventional CPK coloring. (B) Structure of synthesized amphiphilic terephthalates. (C) Schematic model of 2D MOCN at the air–water interface.

microscopy (AFM), and X-ray reflectivity (XRR), we elucidated the structure of the 2D MOCN. Furthermore, we advanced the Langmuir monolayer technique beyond aqueous systems by harnessing coordination-driven self-assembly to form, for the first time, Langmuir monolayers at the air–DMF interface.

2 | Results and Discussion

2.1 | Synthesis of Clusters and Amphiphiles

In this work, we aim to construct a two-component monolayer in which an amphiphilic ligand is spread at the air–water interface, while the second component, **Zr12** or **Hf12** metal oxo clusters, is introduced from the aqueous subphase. Achieving this assembly requires the synthesis of tailor-made amphiphiles and clusters. We synthesized **Zr12**- and **Hf12**-acetate clusters from their respective metal alkoxides according to our previous reports [20]. Pair distribution function (PDF) analysis verified the cluster structure (Figure 1B and Figure S1), consisting of two M_6O_8 cores connected through four intercluster bridging acetates. Inspired by the well-known MOF linker 1,4-benzenedicarboxylic acid (BDC), we developed amphiphilic derivatives that retain the carboxylate coordination sites while incorporating hydrophobic alkyl chains to promote monolayer formation at the air–water interface. Accordingly, we synthesized six amphiphilic terephthalates starting from 2,3-dihydroxyterephthalic acid (Scheme 2). First, the carboxylic acid groups were protected through esterification. Subsequent alkylation of both hydroxyl groups with alkyl halides yielded the methyl ester derivatives of the desired amphiphiles.

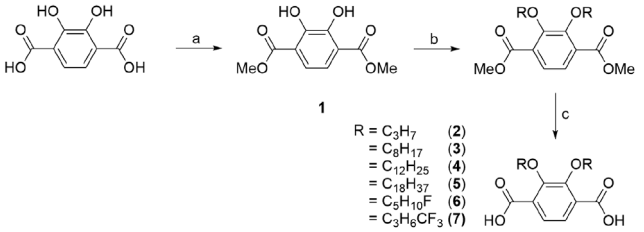

SCHEME 2 | Synthetic route of amphiphilic terephthalic acids. (a) H_2SO_4, methanol, reflux, overnight. (b) 1-haloalkane, K_2CO_3, DMF, 85°C, 3–12 h. (c) KOH, THF/water, reflux, 3–12 h.

Further saponification in basic conditions restored the carboxylate functionality that can be further exploited to coordinate with clusters. Among the synthesized amphiphiles, two possessed fluorinated aliphatic chains (**6**, **7**) to facilitate XPS measurements. All synthesized molecules were characterized with ^{1}H, ^{13}C, ^{19}F NMR, and high-resolution mass spectrometry (HR-MS) (see supporting information).

2.2 | Cluster Stability in Water

Unlike conventional MOCN formation through the Langmuir method, which typically employs simple metal ions as the subphase species, our approach utilizes preformed metal oxo clusters. To ensure the structural integrity of these clusters under the experimental conditions, we evaluated their behavior in water. The clusters were readily soluble in water at 10 mM

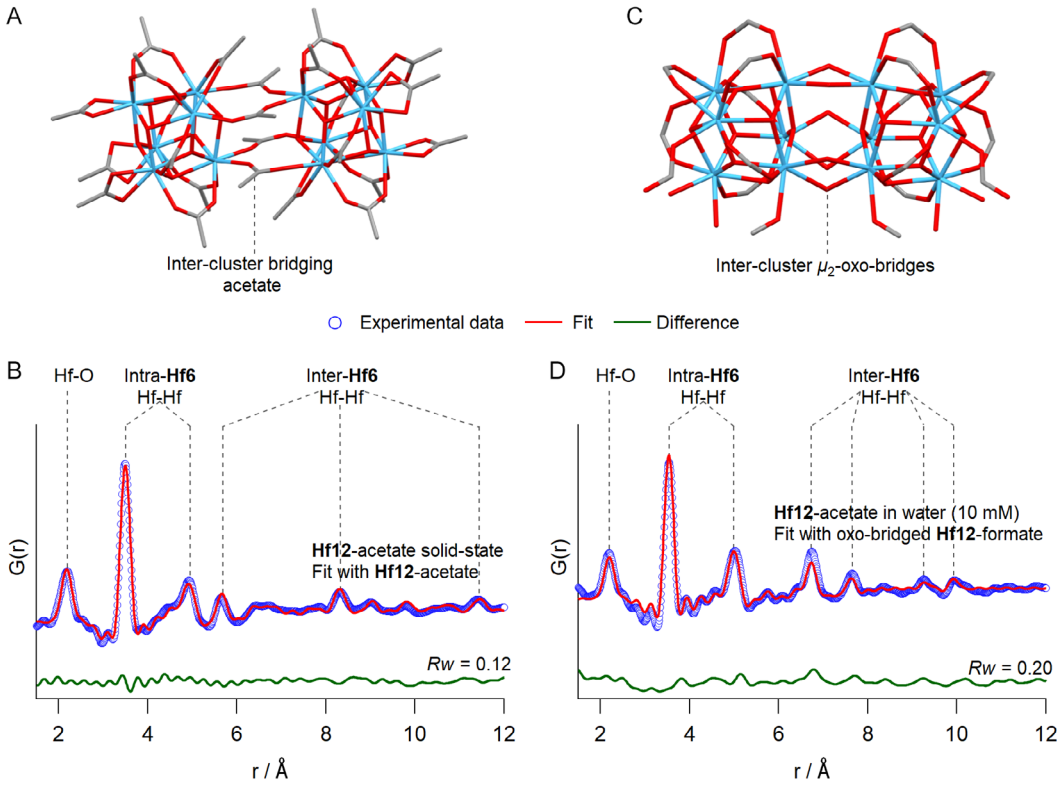

FIGURE 1 | (A) The crystal structure of **Hf12**-acetate cluster. Hydrogen atoms are omitted for clarity. Blue atoms represent hafnium, all other atoms follow conventional CPK coloring. (B) PDF fit for synthesized **Hf12**-acetate cluster in solid-state with its crystal structure. See Table S1 for refined parameters. (C) Structure model of μ_2-oxo-bridged **Hf12**-formate cluster fragmented from the crystal structure of **Zr36**-formate. (D) PDF fit for 10 mM aqueous solution of **Hf12**-acetate cluster with the structure model of μ_2-oxo-bridged **Hf12**-formate. See Table S2 for refined parameters.

concentration, forming a homogeneous acidic solution (pH 3.77). The carboxylate ligands on the cluster can be exchanged with hydroxylates and water molecules according to several reported Zr-based MOFs [52–54]. Hydroxylate ligands can also act as intercluster bridging ligands that connect two **Zr6** monomers [55]. Such ligand-dependent speciation is observed in literature. In the absence of carboxylates, at low pH, Zr(IV) predominantly exists as a tetrameric species - $[Zr_4(OH)_8(OH_2)_{16}]^{8+}$ in water, featuring a square **Zr4** core stabilized by eight bridging μ_2-OH ligands [56]. A stepwise increase in acetic acid concentration and pH cause the **Zr4** species to undergo a structural rearrangement to form a hexanuclear cluster in water [57]. To verify the structural integrity of our **M12** clusters in water, we performed PDF analysis in aqueous solutions. We selected **Hf12** clusters for core characterization due to the higher atomic number and consequently, a higher contrast for X-ray scattering. Surprisingly, the cluster structure changed in water, specifically in the intercluster atomic distances, without altering intra-**Hf6** distances (Figure S2). To elucidate the structural changes in detail, we fitted the experimental data with various models. The best fit was obtained with a **Hf12** structure extracted from the larger structure of **Zr36**-formate (CCDC 2002902), where two **Hf6** monomers are linked through μ_2-oxo bridges, with $Rw = 0.20$ (Figure 1C,D) [58]. The PDF data showed good agreement with other oxo-bridged **Hf12** structure models (Figure S3). Dimerization of **Zr6** units through oxo bridges has been reported for **Zr6**-acetate clusters incubated in water at 60°C [59]. When the inter-cluster bridging acetates were replaced with oxo-bridges, the **Hf6** monomer units come closer, thereby shortening the inter-cluster Hf–Hf distances, as revealed by PDF analysis. Such oxo-bridged **M12** clusters can also act as metal nodes in MOFs [42, 60–62], even with terephthalate linkers forming hexagonal close-packed (*hcp*) **M12**-UiO-66 [63, 64]. We observed the same structural transformation to oxo-bridged clusters when PDF measurements were performed immediately after dissolution or after incubation at room temperature for up to 48 h (Figure S4). We further expanded the PDF analysis to examine the effect of pH and various modulators on cluster structure. Interestingly, the proposed structure remained stable across a pH range of 1–4, despite the presence of concentrated acetic acid, formic acid, or hydrochloric acid (Figure S5). The cluster structure was slightly different below pH 1.

2.3 | Langmuir Monolayer Studies

The interfacial self-assembly properties of amphiphilic terephthalates on pure water and aqueous solution of **Zr12**/**Hf12** acetate clusters were studied using the Langmuir balance technique. 2,3-Dioctyloxyterephthalic acid (**3**) failed to form stable monolayers on pure water as evidenced by the absence of surface pressure increase upon compression (Figure 2A). In contrast, when the subphase was supplemented with a low concentration of oxo clusters (i.e., 10 μM), the terephthalate derivative formed a stable Langmuir monolayer, displaying a collapse pressure as high as 40 mN m^{-1}. The formation of a stable Langmuir monolayer exclusively in the presence of oxo clusters in the subphase strongly supports a mechanism involving ligand exchange, whereby acetate ligands are displaced by terephthalate amphiphiles to enable robust self-assembly. Monolayer formation was further studied by means of BAM. The lack of contrast on micrographs of terephthalate acquired on pure water confirmed its inability to form monolayers at the interface (Figure 2B–D). The presence of zirconium or hafnium acetate clusters in the subphase led to the spontaneous formation of a monolayer even before barrier compression as evidenced by the presence of bright islands, further confirming a ligand exchange-driven assembly mechanism (Figure 2E–G). Subsequent compression brought the monolayer islands closer together until they merged and eventually covered the whole interfacial area.

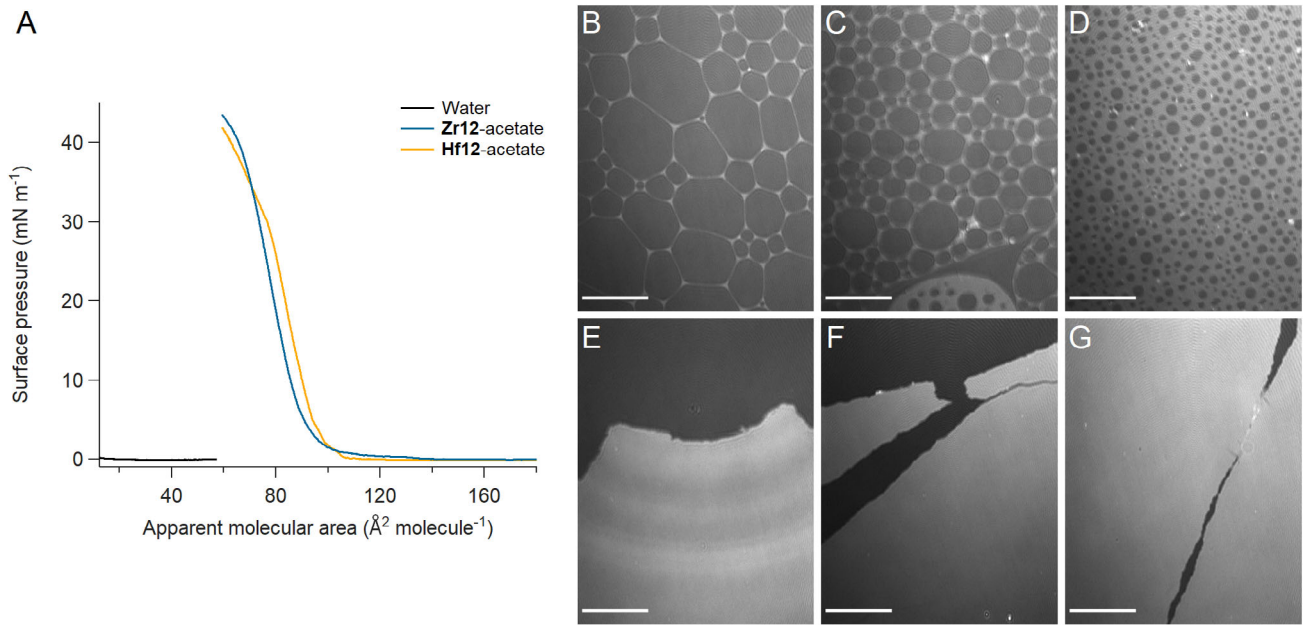

FIGURE 2 | (A) Surface pressure-area compression isotherms of **3** on pure water and on aqueous solutions containing 10 μM of **Zr12** or **Hf12** acetate. BAM micrographs of a monolayer of **3** on pure water (B–D), and on a 10 μM **Zr12**-acetate aqueous solution (E–G), before compression (B, E), at the isotherm takeoff (F), and at a surface pressure of $\pi = 20$ mN m^{-1} (G). Scale bar: 100 μm.

Similar to **3**, the propyl analog (**2**) did not form a monolayer on water but, instead, formed monolayers on cluster solutions (Figure S7). Interestingly, longer aliphatic chain-substituted terephthalic acids, such as 2,3-didodecyloxyterephthalic acid (**4**) and 2,3-dioctadecyloxyterephthalic acid (**5**), were amphiphilic enough to form stable monolayers at the air–water interface. Nonetheless, both also formed rigid self-assembled monolayers on cluster solutions (Figures S8 and S9). Finally, we evaluated the effect of hydrophobic fluorinated analogs. Both 2,3-bis((5-fluoropentyl)oxy)terephthalic acid (**6**) and 2,3-bis(4,4,4-trifluorobutoxy)terephthalic acid (**7**) could not form monolayers on water but formed monolayers on cluster solutions (Figure S10 and S11).

BAM measurements showed that the monolayer morphology on cluster solutions was similar for all the studied amphiphiles. However, slight differences were observed in the Langmuir isotherms, which can be further analyzed using various parameters. From a typical Langmuir isotherm, characteristic values can be extracted to better explain the self-assembly process such as limiting molecular area (A_{limit}), collapse pressure, slope, and static elastic modulus (ε_s) (Figures S12 and S13 and Table S5). Remarkably, the slopes of fluorinated terephthalates were lower than those of their alkylated counterpart, indicating the formation of less rigid layers. They also showed larger molecular areas. The limiting molecular areas were in the range of 60–110 $Å^2$/terephthalate. The broad range can be attributed to the shape of the isotherm and varying slope.

2.4 | Monolayer Characterization

The monomolecular layer of **3** prepared on both **Zr12**-acetate and **Hf12**-acetate was transferred at a surface pressure of 25 mN m^{-1} onto solid substrates (i.e., highly oriented pyrolytic graphite-HOPG and silicon/silicon dioxide coated with octadecyltrichlorosilane-OTS) through the Langmuir–Schaefer (LS) method. Contact angle measurements carried out on layers transferred to OTS-coated-Si substrates showed a static contact angle of 86.6°, which is consistently lower than that of the unmodified substrate (110.6°). This confirmed the successful transfer of the monolayer (Figures S14 and S15). In addition to monolayer transfer, multilayer films were also deposited using the LB method to obtain thicker samples suitable for ToF-SIMS. Ten layers of **3**-**Zr12** and **3**-**Hf12** were deposited on mica substrate at a surface pressure of 25 mN m^{-1}.

The incorporation of **Zr12** clusters into the monolayer was studied by XPS (Figure 3A,B and Figure S16). The Zr3d region exhibited two peaks corresponding to $Zr3d_{5/2}$ and $Zr3d_{3/2}$ located at 182.7 and 185 eV, respectively [65, 66]. Deconvolution of the C1s spectrum revealed peaks assigned to carbonyl carbon (C═O) at 288.8 eV, Zr—O—C at 286.0 eV, and aliphatic C—C at 284.3 eV. The C═O signal could originate from either the acetate ligands on the cluster or amphiphile **3**. To confirm the presence of amphiphiles in the monolayer, XPS analysis was also performed on a monolayer of fluorine-containing terephthalate **7**, prepared on **Zr12**-acetate clusters and transferred onto HOPG at a surface pressure of 25 mN m^{-1}. Both zirconium and fluorine

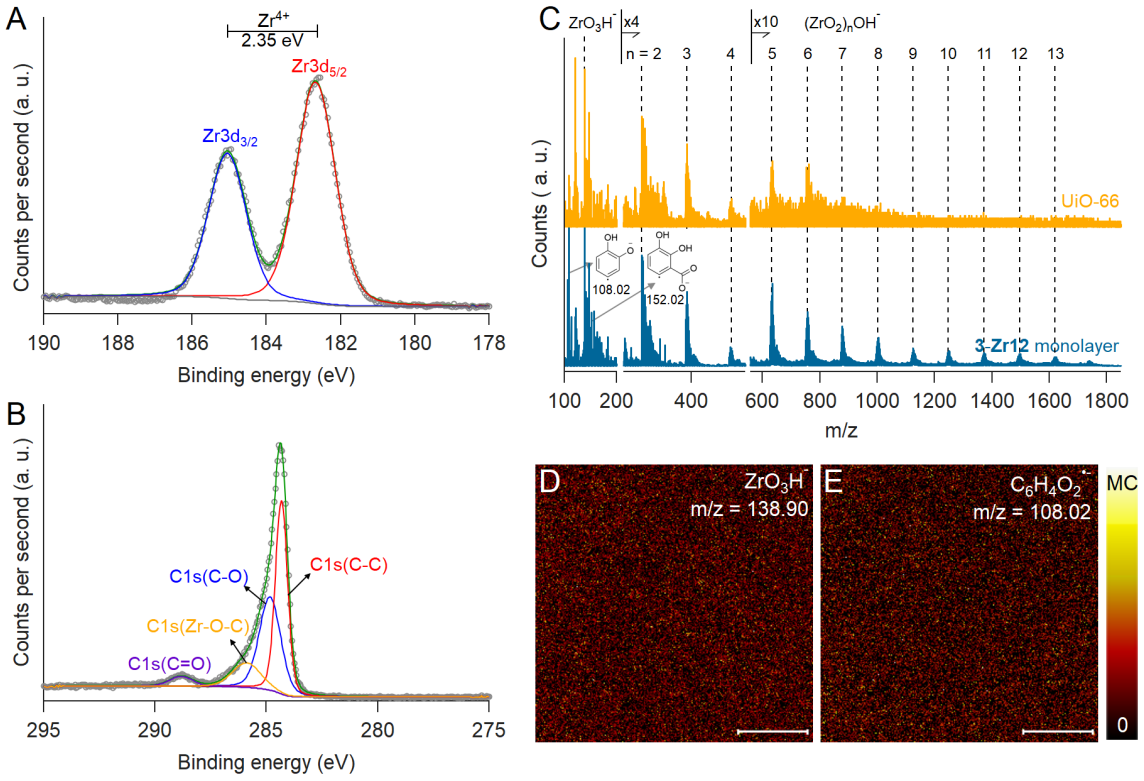

FIGURE 3 | X-ray photoelectron spectra of the monolayer of **3** prepared on **Zr12**-acetate, transferred on HOPG substrate. Both (A) Zr3d and (B) C1s spectra are shown. C1s spectrum is deconvoluted into contributions corresponding to carbon atoms in different chemical environments, including aliphatic/aromatic carbon, C–O-containing species, carbonyl carbon, and carbon atoms associated with Zr–O–C environments. (C) ToF-SIMS negative ion mode spectra of **3**-**Zr12** transferred on mica substrate, with UiO-66 provided as a reference. (D,E) Shows the spatial distribution of ZrO_3H^- and the amphiphile **3** fragment, respectively. Scale bar = 100 μm; MC = maximum counts.

signals were detected, confirming the co-existence of the clusters and amphiphilic molecules within the monolayer structure (Figure S18). The Zr/F ratio was 70:30. However, it should be noted that when covered with a monolayer, the substrate is more hydrophilic, leading to the retention of residual subphase droplets, which may account for an elevated Zr signal. This suggests that the actual Zr/F ratio is likely less than the observed ratio. Zr–O–Zr, Zr–O–C, and carboxylate oxygens were also detected after deconvoluting O1s spectra (Figure S17) [66]. Similar results were obtained for **3**-**Hf12** monolayer, with the Hf4f region showing $Hf4f_{7/2}$ and $Hf4f_{5/2}$ peaks at 17.3 and 19.0 eV, along with analogous C1s and O1s signals (Figure S19).

To verify the chemical composition and spatial distribution of the monolayer, ToF-SIMS analyses were performed. The amphiphile **3** alone, drop-cast on a Si wafer, exhibited both pseudomolecular ions and characteristic fragment ions (Figure S20). Due to extensive ionization and fragmentation inherent to the technique, a multilayer film of **3**-**Zr12** on mica was analyzed instead of a monolayer, as monolayers typically yield low signal intensity owing to the limited amount of analyte within the probing depth. Although species containing both the cluster and amphiphile together could not be detected due to the extensive fragmentation during the analysis, fragments corresponding to individual components were readily observed. As a control, UiO-66 bulk MOF synthesized from $ZrOCl_2{\cdot}8H_2O$ was also drop-cast and analyzed [67]. Notably, zirconium oxo cores appeared as $(ZrO_2)_nH^+$ and $(ZrO_2)_nOH^-$ in positive and negative ion modes, respectively (Figures 3C and S21). For UiO-66, the dominant zirconium oxo fragments correspond to $n \leq 6$, in agreement with the $Zr_6O_4(OH)_4$ node, while higher n-species are strongly suppressed in intensity. In contrast, the MOCN sample exhibited intense signals with n values up to 12, consistent with the presence of dimeric **Zr12** cluster nodes in aqueous solution and in the monolayer, as evidenced by PDF analysis. The presence of amphiphile **3** on the monolayer was identified through characteristic fragment ions at $m/z = 108.02$ (2-hydroxyphenolate radical) and 152.02 (2,3-dihydroxybenzoate radical), see Figure 3C. The ToF-SIMS ion images of ZrO_3H^- and amphiphile **3** fragment ion at $m/z = 108.02$ confirm a homogeneous distribution of both zirconium oxo cluster nodes and amphiphiles across the monolayer, see Figure 3D,E. Analogously, the **3**-**Hf12** layers exhibited hafnium oxo fragments appearing as $(HfO_2)_nH^+$ and $(HfO_2)_nOH^-$ in the positive and negative ion modes, respectively (Figures S22 and S23). Signals with n values up to 12 were observed, consistent with the presence of dimeric **Hf12** cluster nodes, and the corresponding ToF-SIMS ion images confirm a homogeneous lateral distribution of both hafnium oxo clusters and amphiphile **3** across the layer.

Low-dose, cryo-STEM was employed to analyze the morphology of the monolayer. The **3**-**Zr12** monolayer sheets were transferred onto lacey carbon copper TEM grids using the LS method. The illumination and imaging conditions were carefully optimized to enable high-resolution imaging of the monolayer regions. The collection angle of the high-angle annular dark-field (HAADF) detector yielded the prominent atomic number-sensitive image contrast. As shown in Figure 4A, several regions of the monolayer are suspended across the vacuum windows of the lacey carbon grid, confirming the free-standing nature of the film. The cryo-STEM HAADF imaging was complemented by spectrum imaging (SI) using the dedicated SuperX energy-dispersive X-ray spectroscopy (EDS) module of the STEM instrument. The Zr-L_α, O-K_α, and C-K_α signal maps (Figure 4B–E) evidenced the spatial distribution of Zr, O, and C within the monolayer films. The Zr L_α-map traces the spatial distribution of the oxo cluster nodes, while the C K_α-line maps highlight the organic linkers and contributions from the amorphous carbon support. The O K_α-line signal reflects oxygen atoms present in both the nodes and linkers. The correlation of these elemental maps confirms the uniform coverage of the **3**–**Zr12** monolayer across the imaged region. To assess the periodic nature of the layers, atomic-resolution imaging was attempted (Figure 4F). Owing to the high electron-beam sensitivity of the material, even low-dose conditions (<10 pA probe current, 5 ms dwell time, 1k × 1k resolution) led to rapid degradation of the monolayers

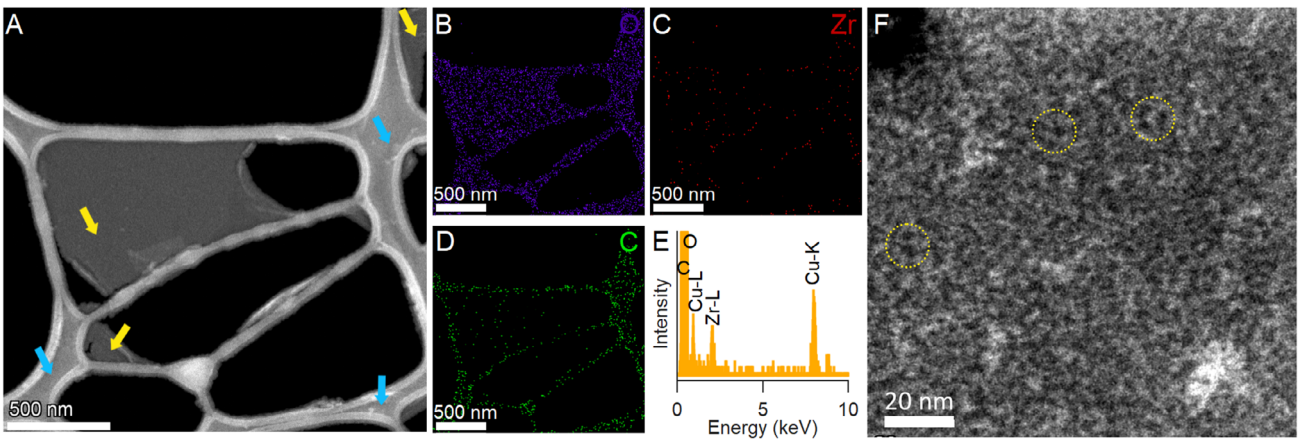

FIGURE 4 | Spectrum image analyses of a representative specimen region. (A) High-angle annular dark-field (HAADF) STEM micrograph of **3**-**Zr12** monolayer. The dark gray areas correspond to the amorphous lacey carbon support, while the black regions represent the vacuum windows in the foil. Yellow arrows highlight the free-standing (suspended over the windows) **3**-**Zr12** monolayer sheet, whereas the blue arrows mark regions of the lacey carbon covered by the monolayer. (B–D) Elemental maps extracted from the spectrum image: (B) O-K_α, (C) Zr-L_α, and (D) C-K_α. Scale bar: 500 nm. (E) EDX spectrum acquired from the entire imaged area. (F) HAADF micrograph of a monolayer region recorded at higher magnification under damage-free conditions (pixel size 130 pm, 1k × 1k resolution, 5 µs dwell time, <10 pA probe current), revealing the quasiperiodic nature of the sheet. Encircled regions highlight repeating structural motifs with characteristic dimensions of 4–5 nm.

at magnifications above 755,000× (Figure S24). As a result, imaging was limited to pixel sizes no smaller than 130 pm, preventing fast Fourier transform (FFT) evaluation and precluding unambiguous crystallographic analysis. Nevertheless, HAADF images acquired at the highest achievable damage-free resolution reveal quasi-periodic contrast along the monolayer sheets (Figure 4F). The observed repeating features have characteristic length scales of approximately 4–5 nm and were consistently detected across multiple cryo-STEM sessions and independent monolayer specimens.

The thickness of the layers was evaluated with ellipsometry. A 20-min UV/ozone treatment of silicon wafers formed a native oxide layer of 1.8 nm, which is in good agreement with the literature [68]. Subsequent treatment with OTS yielded a second layer with a thickness of 2.7 nm. Considering that a fully stretched OTS molecule is 2.64 nm long [69], the observed thickness suggests a well-ordered surface modification. Finally, LS transfer of a **3**-**Zr12** or **3**-**Hf12** monolayer onto the OTS-coated silicon wafer increased the total thickness by approximately 3.1 ± 0.3 nm or 2.8 ± 0.2 nm, respectively, as determined using the Cauchy model, see Figures S25, S26 and Table S6. The refractive index of the monolayer, determined from fitting, was 1.4 ± 0.1, which is consistent with literature values reported for UiO-66 [70]. Consistent with ellipsometry measurements, AFM images confirmed that the monolayer has a thickness of approximately 3 nm (Figure 5A and Figure S27). A zoomed-in micrograph reveals surface features of the monolayer, showing a roughness of up to 1.5 nm (Figure 5B). To gain insight into the monolayer structure at the interface prior to transfer, we performed synchrotron XRR measurements (Figure 5C). The monolayer of **3** on 10 µM **Zr12**-acetate subphase at a surface pressure of 10 mN m^{-1} can be described by a simple single-layer model, with a thickness of 11.41 ± 0.16 Å and an average scattering length density (SLD) of 18.85 ± 0.28 × 10^{-6} $Å^{-2}$. Importantly, the thickness obtained from XRR corresponds only to the portion of the monolayer protruding above the aqueous subphase, while the model does not fully capture contributions from the cluster core extending into the water. Similar underestimations of thickness for submerged or partially buried features have been reported in XRR studies of nanoparticle monolayers [71–73]. Nonetheless, the average SLD reflects contributions from the **Zr12** cluster, terephthalate linker, and octyl chains (See Figure S28 and Table S7 for detailed calculations). The method of average SLD has previously been applied to azobenzene glycolipids, where the relatively low contrast compared to phospholipids prevented clear resolution of distinct boundaries between the head and tail regions [74]. In addition, the cluster-containing subphase exhibits a slightly higher SLD (10.18 ± 0.03 × 10^{-6} $Å^{-2}$) compared

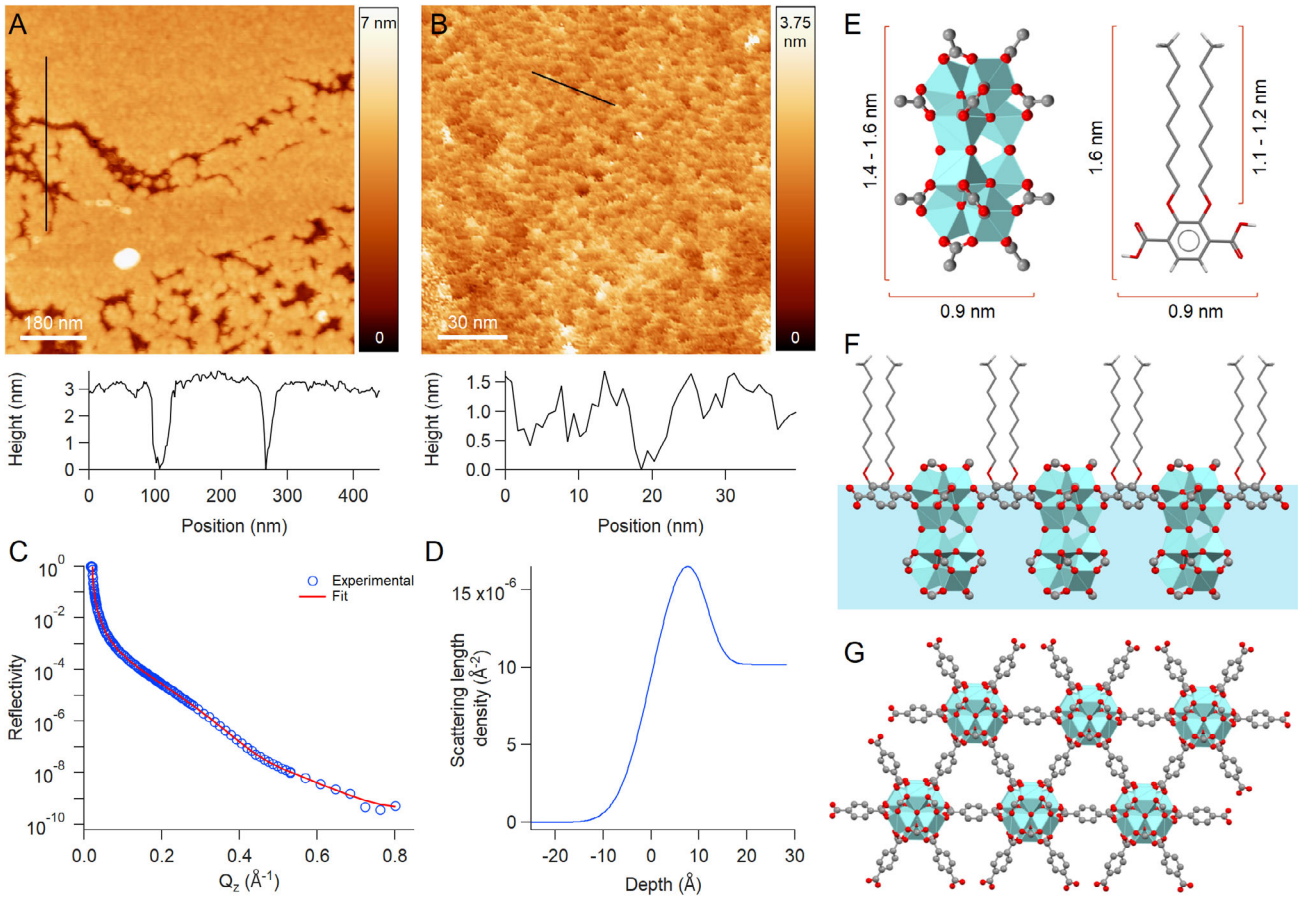

FIGURE 5 | (A) AFM micrograph of the **3**-**Zr12** monolayer transferred onto an OTS-coated silicon wafer. (B) Magnified view of a selected region. The overlaid lines in both images indicate the positions of the line profiles shown below, highlighting the height variations across the monolayer. (C) X-ray reflectivity curve and fit of **3**-**Zr12** monolayer on 10 µM **Zr12**-acetate subphase at a surface pressure of 10 mN m^{-1}. The corresponding depth profile is shown in (D). (E) Molecular dimensions of oxo-bridged **Zr12** cluster node and amphiphile **3**. (F) Side view and (G) top view of the proposed packing model for the monolayer.

to pure water, reflecting the contribution of dissolved cluster units. The depth profile of the SLD and fitting parameters are given in Figure 5D and Table S8, respectively.

Combining the compositional information obtained from PDF, XPS, and ToF-SIMS, and with the height analysis from ellipsometry, AFM, and reflectivity, we propose a packing model for the self-assembled MOCN monolayer (Figure 5F,G). The structure model was derived from *hcp*-UiO-66, where oxo-bridged **Zr12** cluster nodes are connected through terephthalate linkers [64]. Unlike **Zr6**-UiO-66, a single layer of *hcp*-UiO-66 can be confined within a plane as a monolayer. The long aliphatic chains protrude outward from the interface, while the planar *hcp*-UiO-66 layer forms the observed monolayer. Each **Zr12** node is coordinated to six terephthalate linkers, corresponding to a theoretical molecular area of 67 $Å^2$ per linker. This value aligns closely with the limiting molecular areas (A_{limit}) of 62.2 and 60.1 $Å^2$/terephthalate observed for **2**-**Zr12** and **2**-**Hf12**, respectively, in Langmuir monolayer studies, which further confirms the structure model. While our investigations at the air–water interface revealed the coordination-driven nature of monolayer self-assembly, the spontaneous monolayer formation immediately after spreading the amphiphile suggests a distinct kinetics governing the assembly process. As all our experimental results are consistent with monolayer formation being driven primarily by coordination rather than amphiphilic self-assembly, we sought to evaluate whether such monolayers could also form at the surface of an organic solvent with reduced polarity. This system offers a contrasting environment to assess the generality of the coordination-driven assembly process.

2.5 | Monolayers on DMF

DMF is a critical solvent in the synthesis of group 4 MOFs due to its ability to coordinate with metal centers, hydrolyze to regulate the acidity of the reaction medium, and direct the assembly of the framework structures [75, 76]. The formation and stabilization of **Zr6** SBUs have been demonstrated in DMF at room temperature [77]. Given that bulk UiO-66 crystallizes and remains insoluble in DMF, a monomolecular layer of a similar system is also expected to remain stable in DMF. Here, we extended our Langmuir monolayer experiments—originally performed on water to DMF, which is an unusual medium for Langmuir studies. Although Langmuir monolayers on nonaqueous subphases are extremely rare, a few reports exist. For example, iron oxide nanoparticle monolayers were formed at the air–dimethylsulfoxide (DMSO) interface through drop-casting method [78]. The classic criterion for the formation of a Langmuir monolayer is that the amphiphile should be insoluble or sparingly soluble in the subphase [79]. The insolubility ensures that the amphiphile is confined at the air–liquid interface. When amphiphiles are too soluble, they tend to dissolve into the bulk, preventing monolayer formation under equilibrium conditions. We found that our amphiphile **3** is highly soluble in DMF, with solubility exceeding 100 g L^{-1}.

Coordination-driven self-assembly demonstrated above can be used to "lock" soluble amphiphiles at the interface before they diffuse into the subphase. The strategy relies on the kinetics of coordination being faster than the kinetics of dissolution. Tuccitto et al. demonstrated that Co^{2+} ions can prevent the hydrolysis of diiminic ligand to dialdehydic compound and subsequent dissolution into the aqueous subphase [80]. In their study, diimine amphiphiles formed monolayers at the air–water interface but progressively hydrolyzed into dialdehydes, decreasing the surface pressure. Coordination with Ni^{2+} stabilized the imine functionalities and effectively trapped the ligands at the interface. Nickel coordination can also suppress the slower dissolution of amphiphilic cyanoferrate complexes by forming stable 2D networks [81]. Herein, we report the first example of a Langmuir monolayer formed at the air–DMF interface using an amphiphile soluble in DMF.

PDF analysis of a 10 mM solution of **Hf12**-acetate clusters in an 80:20 DMF/water mixture revealed the same oxo-bridged dimeric **Hf12** structure as observed in pure water, confirming that the presence of a high concentration of DMF does not alter the cluster structure (Figure S29). Langmuir monolayer studies were performed at the air–DMF interface using the Langmuir balance method. 10 μM solution of **Zr12**-acetate cluster in DMF (with 0.06% water) served as the subphase, while the amphiphile **3** was spread at the interface as a solution in THF/diethyl ether (1:4, 1 mg mL^{-1}). The surface pressure-area isotherm measured is shown in Figure 6A. The shape of the isotherm closely resembles that obtained at the air–water interface. However, the collapse pressure was reduced to approximately one-quarter of the value observed on water, which can be attributed to the lower surface tension of DMF (37.1 mN m^{-1} at 20 °C) compared to water (72.8 mN m^{-1} at 20 °C) [82]. Moreover, a 3–4-fold decrease in the apparent molecular area per terephthalate unit was observed, indicating partial dissolution of the amphiphile into the DMF subphase. A comparable phenomenon was reported by Tuccitto et al., who observed that 64%–75% of the amphiphile hydrolyzed and dissolved into the subphase without coordinating to metal ions [80]. Despite this solubility, a fraction of the amphiphile is locked at the interface due to coordination with **Zr12** oxo clusters, resulting in the formation of a stable interfacial monolayer.

BAM was used to image the monolayers at the air–DMF interface. Considering the refractive index of DMF (1.43 at 20°C), the Brewster angle was adjusted to 55° (See Figure S30). The resulting BAM micrographs (Figure 6B,C) revealed rigid monolayers, comparable to those obtained at the air–water interface. The monolayers were subsequently transferred onto OTS-coated Si wafers using the LS method at a surface pressure of 5 mN m^{-1}. Successful transfer was confirmed by contact angle measurements (Figure S31), after which the deposited monolayers were subjected to compositional and height analyses. XPS spectra of the Zr3d, C1s, and O1s regions were consistent with those obtained for monolayers prepared at the air–water interface. Importantly, no signals were detected in the 390–405 eV range, confirming the absence of N1s contributions and indicating that no residual DMF remained in the monolayer (Figures 6D and S32). Further confirmation of the monolayer composition was obtained from ToF-SIMS measurements, which identified characteristic **Zr12** nodes (Figure S33). Finally, AFM and ellipsometry revealed a layer thickness of approximately 3 nm, in good agreement with the thickness observed for monolayers formed at the air–water interface (Figures 6E, and S34, Table S10). Collectively, these results demonstrate that monolayers formed at the air–DMF interface adopt a structural model analogous to those prepared at the air–water interface.

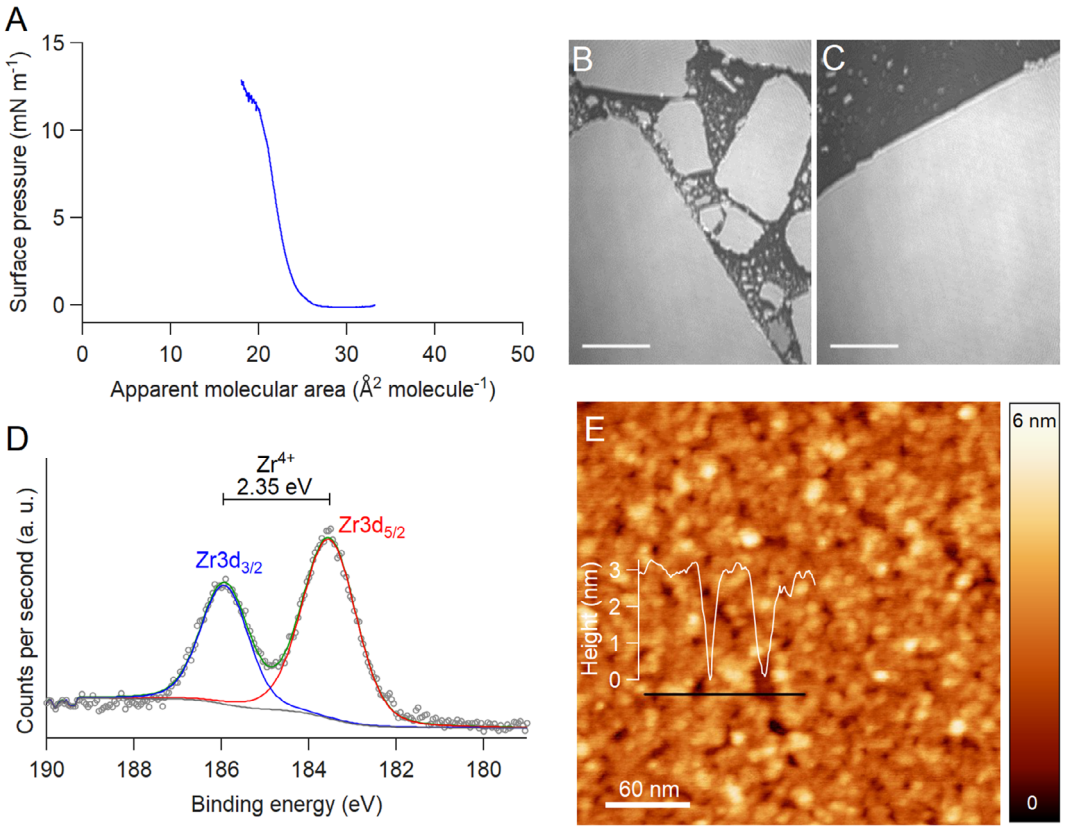

FIGURE 6 | (A) Surface pressure-area compression isotherm and (B,C) BAM micrographs of the monolayer of **3** on 10 μM **Zr12**-acetate solution in DMF, recorded at the isotherm takeoff (B), and at a surface pressure of $\pi = 5$ mN m^{-1} (C). Scale bar: 100 μm. (D) X-ray photoelectron spectra (Zr3d region) of **3**-**Zr12** monolayer formed at the air–DMF interface, transferred on OTS-coated silicon wafer. (E) AFM micrograph of the **3**-**Zr12** monolayer transferred from the air–DMF interface onto an OTS-coated silicon wafer, with corresponding height analysis.

Both DMF and water are known to coordinate to **Zr6** oxo clusters through oxygen atoms, effectively acting as ligands. For instance, milling of **Zr6**-methacrylate cluster with DMF results in the formation of $Zr_6O_4(OH)_4(OMc)_{12}(DMF)_4$ crystals [27]. Likewise, numerous **Zr6** clusters have been reported with water in the coordination shell [83–86]. In addition to coordination, both DMF and water are capable of forming hydrogen bonds with the Zr-OH of the bulk UiO-66 node [87]. Given that the monolayer structure closely resembles a 2D analog of *hcp*-UiO-66, we propose that similar interactions between the subphase and the 2D framework—either via coordination or hydrogen bonding—stabilize the monolayer at both air–water and air–DMF interface.

An analogy can be drawn between the solvothermal synthesis of MOFs and the interfacial formation of 2D MOCNs. In conventional solvothermal synthesis, zirconium precursors and terephthalic acid linkers are dissolved in DMF in the presence of modulators (e.g., acetic acid, formic acid, or hydrochloric acid). Upon heating, this homogeneous solution yields bulk UiO-66 crystallites, which are insoluble in DMF. Similarly, when preformed **Zr12** SBUs are dissolved in DMF and amphiphilic terephthalate ligands are spread at the liquid interface, coordination leads to the formation of a 2D UiO-66-type sheet. The hydrophobic alkyl chains on the ligands inhibit out-of-plane growth, thus confining crystallization to a monolayer at the interface. Acetate ligands of **Zr12** exchanged with oxo bridges get released into the solution, and may act as modulators. While the bulk MOF formed under solvothermal conditions represents a thermodynamic product, the interfacial monolayer is considered a kinetic product stabilized by spatial constraints and amphiphilic interactions.

3 | Conclusion

We investigated the speciation behavior of **Zr12**- and **Hf12**-acetate clusters in aqueous media, revealing that intercluster bridging carboxylates undergo exchange with oxo-bridges. The resulting oxo-bridged **Zr12** clusters act as SBUs of *hcp*-UiO-66, enabling the formation of the first 2D metal–organic coordination network consisting of a single sheet of *hcp*-UiO-66 at the air–water interface. This also represents the first example of a Langmuir monolayer incorporating metal oxo clusters, rather than single metal ions. The monolayers were successfully transferred onto various solid substrates using Langmuir–Blodgett and Langmuir–Schaefer techniques, preserving their structural integrity. We further extended the methodology to DMF, reporting the first Langmuir monolayer formed at the air–DMF interface. The behavior on DMF revealed the coordination-driven self-assembly nature of the monolayer, drawing a clear analogy to the solvothermal synthesis of UiO-66. While the latter yields thermodynamic bulk crystallites, the interfacial monolayer represents a kinetic product stabilized by amphiphilic surface confinement. These findings offer a foundation for the interfacial fabrication of 2D MOF-like networks using preformed oxo clusters and open

new directions in the design of self-assembled monolayers, with future efforts aimed at enhancing intrinsic stability to enable more definitive structural characterization and broaden potential applications.

Author Contributions

Ajmal Roshan Unniram Parambil: investigation (lead), visualization (lead), data curation (lead), formal analysis (lead), writing – original draft (lead). **Muhammed Jibin Parammal:** investigation (supporting). **Prashant Hitaishi:** formal analysis (supporting). **Seyed Amirabbas Nazemi:** investigation (supporting). **Narmadha Devi Suresh Kumar:** investigation (supporting). **Alla Sologubenko:** investigation (supporting), formal analysis (supporting). **Stephan Handschin:** investigation (supporting). **Bridget M. Murphy:** data curation (supporting). **Thomas A. Jung:** data curation (supporting), writing – review & editing (supporting). **Jonathan De Roo:** supervision (equal), funding acquisition (equal), conceptualization (equal), writing – review & editing (supporting). **Patrick Shahgaldian:** conceptualization (lead), funding acquisition (lead), project administration (lead), validation (lead), supervision (lead), writing – original draft (supporting), writing – review & editing (lead).

Acknowledgments

Support from the Swiss Nanoscience Institute (Project P2006) and the Swiss National Science Foundation (Project 218106) is gratefully acknowledged. The authors thank Timm Hettich, Michael Pfeffer, and Sylvie Mittelheisser for support with mass spectrometry. We acknowledge the Nano Imaging Lab at the Swiss Nanoscience Institute, University of Basel, as well as Monica Schönenberger for assistance with AFM imaging. The authors are also grateful to Tingting Fu (University of Geneva) for conducting the ToF-SIMS measurements. This research used resources 28-ID-1 of the National Synchrotron Light Source II, a U.S. Department of Energy (DOE) Office of Science User Facility operated for the DOE Office of Science by Brookhaven National Laboratory under Contract No. DE-SC0012704. The authors acknowledge DESY (Hamburg, Germany), a member of the Helmholtz Association HGF, for the provision of experimental facilities. Parts of this research were carried out at PETRA III, and the authors would like to thank Dr Ann-Christin Dippel for assistance in using beamline P21.1. Beamtime was allocated for proposal I-20231114 EC. XRR experiments were also carried out at PETRA III, and the authors would like to thank Chen Shen for assistance at beamline P08. The LISA instrument at P08 is funded by the ErUM-Pro programme (05K16FK1/05K19FK2/05K22FK3) of the German Federal Ministry of Education and Research (BMBF). Beamtime was allocated for proposal I-20230273 EC. The authors also thank Jikson Pulparayil Mathew, Dietger Van den Eynden, and Arnau Roig for assistance with XRR and Langmuir experiments, as well as Aisha Ahsan for fruitful discussions.

Open access publishing facilitated by Fachhochschule Nordwestschweiz FHNW, as part of the Wiley - Fachhochschule Nordwestschweiz FHNW agreement via the Consortium Of Swiss Academic Libraries.

Funding

This study was supported by the Swiss Nanoscience Institute (P2006) and the Swiss National Science Foundation (218106).

Conflicts of Interest

The authors declare no conflicts of interest.

Data Availability Statement

The data underlying the figures are available on the Zenodo platform, DOI: https://doi.org/10.5281/zenodo.17187398.

References

1. H. Furukawa, K. E. Cordova, M. O'Keeffe, and O. M. Yaghi, "The Chemistry and Applications of Metal-Organic Frameworks," *Science* 341 (2013): 1230444.

2. W. Song, Z. Zheng, A. H. Alawadhi, and O. M. Yaghi, "MOF Water Harvester Produces Water from Death Valley Desert Air in Ambient Sunlight," *Nature Water* 1 (2023): 626–634.

3. A. U. Czaja, N. Trukhan, and U. Müller, "Industrial Applications of Metal–Organic Frameworks," *Chemical Society Reviews* 38 (2009): 1284.

4. M. Peplow, "Materials Science: The Hole Story," *Nature* 520 (2015): 148–150.

5. C. Shi, M. S. Duyar, X. Wang, S. Ye, M. Hu, and J. Liu, "Design of Two-Dimensional Metal–organic Framework Nanosheets for Emerging Applications," *FlatChem* 29 (2021): 100287.

6. K. Zhao, W. Zhu, S. Liu, et al., "Two-Dimensional Metal–organic Frameworks and Their Derivatives for Electrochemical Energy Storage and Electrocatalysis," *Nanoscale Advances* 2 (2020): 536–562.

7. G. Chakraborty, I.-H. Park, R. Medishetty, and J. J. Vittal, "Two-Dimensional Metal-Organic Framework Materials: Synthesis, Structures, Properties and Applications," *Chemical Reviews* 121 (2021): 3751–3891.

8. B. Zhang, Z. Qi, Z. Wu, et al., "Defect-Rich 2D Material Networks for Advanced Oxygen Evolution Catalysts," *ACS Energy Letters* 4 (2019): 328–336.

9. Q. Zuo, T. Liu, C. Chen, et al., "Ultrathin Metal–Organic Framework Nanosheets with Ultrahigh Loading of Single Pt Atoms for Efficient Visible-Light-Driven Photocatalytic H_2 Evolution," *Angewandte Chemie International Edition* 58 (2019): 10198–10203.

10. N. D. Savić, K. Declerck, R. R. Prasad, G. Kalandia, J. A. Foster, and T. N. Parac-Vogt, "Programmable 2D Metal-Organic Framework Nanosheets for Enzyme-Like Hydrolysis of Large Proteins," *Advanced Functional Materials* 35 (2025): 2504117.

11. R. Xu, Z. Cai, G. Lan, and W. Lin, "Metal–Organic Layers Efficiently Catalyze Photoinduced Polymerization under Visible Light," *Inorganic Chemistry* 57 (2018): 10489–10493.

12. L. Sun, M. G. Campbell, and M. Dincă, "Electrically Conductive Porous Metal–Organic Frameworks," *Angewandte Chemie International Edition* 55 (2016): 3566–3579.

13. J. Nicks, K. Sasitharan, R. R. Prasad, D. J. Ashworth, and J. A. Foster, "Metal–Organic Framework Nanosheets: Programmable 2D Materials for Catalysis, Sensing, Electronics, and Separation Applications," *Advanced Functional Materials* 31 (2021): 2103723.

14. S. Yuan, J.-S. Qin, C. T. Lollar, and H.-C. Zhou, "Stable Metal–Organic Frameworks with Group 4 Metals: Current Status and Trends," *ACS Central Science* 4 (2018): 440–450.

15. R. T. Jerozal, T. A. Pitt, S. N. MacMillan, and P. J. Milner, "High-Concentration Self-Assembly of Zirconium- and Hafnium-Based Metal–Organic Materials," *Journal of the American Chemical Society* 145 (2023): 13273–13283.

16. A. J. Howarth, Y. Liu, P. Li, et al., "Chemical, Thermal and Mechanical Stabilities of Metal–Organic Frameworks," *Nature Reviews Materials* 1 (2016): 15018.

17. H. Furukawa, F. Gándara, Y.-B. Zhang, et al., "Water Adsorption in Porous Metal–Organic Frameworks and Related Materials," *Journal of the American Chemical Society* 136 (2014): 4369–4381.

18. J. H. Cavka, S. Jakobsen, U. Olsbye, et al., "A New Zirconium Inorganic Building Brick Forming Metal Organic Frameworks with Exceptional Stability," *Journal of the American Chemical Society* 130 (2008): 13850–13851.

19. D. Van den Eynden, R. Pokratath, and J. De Roo, "Nonaqueous Chemistry of Group 4 Oxo Clusters and Colloidal Metal Oxide Nanocrystals," *Chemical Reviews* 122 (2022): 10538–10572.

20. D. Van den Eynden, R. Pokratath, J. P. Mathew, E. Goossens, K. De Buysser, and J. De Roo, "Fatty Acid Capped, Metal Oxo Clusters as the Smallest Conceivable Nanocrystal Prototypes," *Chemical Science* 14 (2023): 573–585.

21. A. R. Unniram Parambil, J. Pulparayil Mathew, M. J. Parammal, and J. De Roo, "M_6O_8 Metal Oxo Clusters: A Key Structural Motif across the Periodic Table," *Coordination Chemistry Reviews* 546 (2026): 216967.

22. A. R. Unniram Parambil, R. Pokratath, M. J. Parammal, et al., "Atomically Precise Surface Chemistry of Zirconium and Hafnium Metal Oxo Clusters beyond Carboxylate Ligands," *Chemical Science* 15 (2024): 17380–17396.

23. U. Schubert, "Cluster-Based Inorganic–organic Hybrid Materials," *Chemical Society Reviews* 40 (2011): 575–582.

24. C. Wang, J. Yan, S. Chen, and Y. Liu, "High-Valence Metal-Organic Framework Materials Constructed from Metal-Oxo Clusters: Opportunities and Challenges," *ChemPlusChem* 88 (2023): e202200462.

25. V. Guillerm, S. Gross, C. Serre, T. Devic, M. Bauer, and G. Férey, "A Zirconium Methacrylate Oxocluster as Precursor for the Low-Temperature Synthesis of Porous Zirconium(IV) Dicarboxylates," *Chemical Communication* 46 (2010): 767–769.

26. A. A. Bezrukov, K. W. Törnroos, E. Le Roux, and P. D. C. Dietzel, "Incorporation of an Intact Dimeric Zr_{12} Oxo Cluster from a Molecular Precursor in a New Zirconium Metal–Organic Framework," *Chemical Communications* 54 (2018): 2735–2738.

27. A. M. Fidelli, B. Karadeniz, A. J. Howarth, et al., "Green and Rapid Mechanosynthesis of High-Porosity NU- and UiO-Type Metal–Organic Frameworks," *Chemical Communications* 54 (2018): 6999–7002.

28. K. Užarević, T. C. Wang, S.-Y. Moon, et al., "Mechanochemical and Solvent-Free Assembly of Zirconium-Based Metal–organic Frameworks," *Chemical Communications* 52 (2016): 2133–2136.

29. B. Karadeniz, A. J. Howarth, T. Stolar, et al., "Benign by Design: Green and Scalable Synthesis of Zirconium UiO-Metal–Organic Frameworks by Water-Assisted Mechanochemistry," *ACS Sustainable Chemistry & Engineering* 6 (2018): 15841–15849.

30. S. Dai, C. Simms, I. Dovgaliuk, et al., "Monodispersed MOF-808 Nanocrystals Synthesized via a Scalable Room-Temperature Approach for Efficient Heterogeneous Peptide Bond Hydrolysis," *Chemistry of Materials* 33 (2021): 7057–7066.

31. F. E. Salvador, V. Miller, K. Shimada, et al., "Mechanochemistry of Group 4 Element-Based Metal–Organic Frameworks," *Inorganic Chemistry* 60 (2021): 16079–16084.

32. R. Dai, F. Peng, P. Ji, et al., "Electron Crystallography Reveals Atomic Structures of Metal–Organic Nanoplates with $M_{12}(\mu_3\text{-O})_8(\mu_3\text{-OH})_8(\mu_2\text{-OH})_6$ (M = Zr, Hf) Secondary Building Units," *Inorganic Chemistry* 56 (2017): 8128–8134.

33. J. Ma, A. G. Wong-Foy, and A. J. Matzger, "The Role of Modulators in Controlling Layer Spacings in a Tritopic Linker Based Zirconium 2D Microporous Coordination Polymer," *Inorganic Chemistry* 54 (2015): 4591–4593.

34. X. Hu, Z. Wang, B. Lin, et al., "Two-Dimensional Metal-Organic Layers as a Bright and Processable Phosphor for Fast White-Light Communication," *Chemistry – A European Journal* 23 (2017): 8390–8394.

35. Z. Hu, E. M. Mahdi, Y. Peng, et al., "Kinetically Controlled Synthesis of Two-Dimensional Zr/Hf Metal–organic Framework Nanosheets via a Modulated Hydrothermal Approach," *Journal of Materials Chemistry A* 5 (2017): 8954–8963.

36. R. Xu, T. Drake, G. Lan, and W. Lin, "Metal-Organic Layers Catalyze Photoreactions without Pore Size and Diffusion Limitations," *Chemistry – A European Journal* 24 (2018): 15772–15776.

37. T. He, B. Ni, S. Zhang, et al., "Ultrathin 2D Zirconium Metal–Organic Framework Nanosheets: Preparation and Application in Photocatalysis," *Small* 14 (2018): 1703929.

38. Z. Lin, N. C. Thacker, T. Sawano, et al., "Metal–Organic Layers Stabilize Earth-Abundant Metal–Terpyridine Diradical Complexes for Catalytic C–H Activation," *Chemical Science* 9 (2018): 143–151.

39. L. Cao, Z. Lin, F. Peng, et al., "Self-Supporting Metal–Organic Layers as Single-Site Solid Catalysts," *Angewandte Chemie International Edition* 55 (2016): 4962–4966.

40. W. Shi, L. Cao, H. Zhang, et al., "Surface Modification of Two-Dimensional Metal–Organic Layers Creates Biomimetic Catalytic Microenvironments for Selective Oxidation," *Angewandte Chemie International Edition* 56 (2017): 9704–9709.

41. J. Chen, Z. Ye, P. Chen, et al., "Two-Dimensional Metal–organic Layers Constructed from Hf_6/Hf_{12}-Oxo Clusters and a Trigonal Pyramidal Phosphine Oxide Ligand," *Dalton Transactions* 51 (2022): 11236–11240.

42. M. J. Cliffe, E. Castillo-Martínez, Y. Wu, et al., "Metal–Organic Nanosheets Formed via Defect-Mediated Transformation of a Hafnium Metal–Organic Framework," *Journal of the American Chemical Society* 139 (2017): 5397–5404.

43. X. Zhang, P. Zhang, C. Chen, et al., "Fabrication of 2D Metal–Organic Framework Nanosheets with Tailorable Thickness Using Bio-based Surfactants and Their Application in Catalysis," *Green Chemistry* 21 (2019): 54–58.

44. J. Yan, Y. Sun, T. Ji, C. Zhang, L. Liu, and Y. Liu, "Room-Temperature Synthesis of Defect-Engineered Zirconium-MOF Membrane Enabling Superior CO_2/N_2 Selectivity with Zirconium-Oxo Cluster Source," *Journal of Membrane Science* 653 (2022): 120496.

45. Y. Zheng, F.-Z. Sun, X. Han, J. Xu, and X.-H. Bu, "Recent Progress in 2D Metal-Organic Frameworks for Optical Applications," *Advanced Optical Materials* 8 (2020): 2000110.

46. L. Wang, H. Sahabudeen, T. Zhang, and R. Dong, "Liquid-Interface-Assisted Synthesis of Covalent-Organic and Metal-Organic Two-Dimensional Crystalline Polymers," *npj 2D Materials and Applications* 2 (2018): 26.

47. R. Dong, T. Zhang, and X. Feng, "Interface-Assisted Synthesis of 2D Materials: Trend and Challenges," *Chemical Reviews* 118 (2018): 6189.

48. R. Dong, M. Pfeffermann, H. Liang, et al., "Large-Area, Free-Standing, Two-Dimensional Supramolecular Polymer Single-Layer Sheets for Highly Efficient Electrocatalytic Hydrogen Evolution," *Angewandte Chemie International Edition* 54 (2015): 12058–12063.

49. R. Makiura, S. Motoyama, Y. Umemura, H. Yamanaka, O. Sakata, and H. Kitagawa, "Surface Nano-Architecture of a Metal–organic Framework," *Nature Materials* 9 (2010): 565–571.

50. M. Moradi, L. G. Tulli, J. Nowakowski, M. Baljozovic, T. A. Jung, and P. Shahgaldian, "Two-Dimensional Calix[4]arene-based Metal–Organic Coordination Networks of Tunable Crystallinity," *Angewandte Chemie International Edition* 56 (2017): 14395–14399.

51. M. Moradi, N. L. Lengweiler, C. E. Housecroft, et al., "Coordination-Driven Monolayer-to-Bilayer Transition in Two-Dimensional Metal–Organic Networks," *The Journal of Physical Chemistry B* 125 (2021): 4204–4211.

52. J. E. Mondloch, W. Bury, D. Fairen-Jimenez, et al., "Vapor-Phase Metalation by Atomic Layer Deposition in a Metal–Organic Framework," *Journal of the American Chemical Society* 135 (2013): 10294–10297.

53. M. Lammert, H. Reinsch, C. A. Murray, M. T. Wharmby, H. Terraschke, and N. Stock, "Synthesis and Structure of Zr(IV)- and Ce(IV)-Based CAU-24 with 1,2,4,5-Tetrakis(4-Carboxyphenyl)benzene," *Dalton Transactions* 45 (2016): 18822–18826.

54. W. Morris, B. Volosskiy, S. Demir, et al., "Synthesis, Structure, and Metalation of Two New Highly Porous Zirconium Metal–Organic Frameworks," *Inorganic Chemistry* 51 (2012): 6443–6445.

55. P. Piszczek, A. Radtke, A. Wojtczak, T. Muzioł, and J. Chojnacki, "Synthesis, Structure Characterization and Thermal Properties of $[Zr_6(\mu_3\text{-}O)4(\mu_3\text{-}OH)_4(OOCCH_2{}^tBu)_9(\mu_2\text{-}OH)_3]_2$," *Polyhedron* 28 (2009): 279–285.

56. M. Kløve, R. S. Christensen, I. G. Nielsen, et al., "Zr^{4+} Solution Structures from Pair Distribution Function Analysis," *Chemical Science* 13 (2022): 12883–12891.

57. C. Hennig, S. Weiss, W. Kraus, J. Kretzschmar, and A. C. Scheinost, "Solution Species and Crystal Structure of Zr(IV) Acetate," *Inorganic Chemistry* 56 (2017): 2473–2480.

58. J. I. Choi, D. Moon, and H. Chun, "Static and Dynamic Adsorptions of Water Vapor by Cyclic $[Zr_{36}]$ Clusters: Implications for Atmospheric Water Capture Using Molecular Solids," *Bulletin of the Korean Chemical Society* 42 (2021): 294–302.

59. Kilian Declerck, Nada D. Savic, Mhamad Aly Moussawi, et al., "Molecular Insights into Sequence-Specific Protein Hydrolysis by a Soluble Zirconium-Oxo Cluster Catalyst," *Journal of the American Chemical Society* 146 (2024): 11400–11410.

60. X. Chen, Y. Lyu, Z. Wang, X. Qiao, B. C. Gates, and D. Yang, "Tuning $Zr_{12}O_{22}$ Node Defects as Catalytic Sites in the Metal–Organic Framework hcp UiO-66," *ACS Catalysis* 10 (2020): 2906–2914.

61. S. S. Boyadjieva, F. C. N. Firth, M. R. Alizadeh Kiapi, et al., "Modulated Self-Assembly of hcp Topology MOFs of Zr/Hf and the extended 4,4′-(ethyne-1,2-diyl)dibenzoate Linker," *CrystEngComm* 25 (2023): 2119–2124.

62. S. Waitschat, H. Reinsch, M. Arpacioglu, and N. Stock, "Direct Water-Based Synthesis and Characterization of New Zr/Hf-MOFs with Dodecanuclear Clusters as IBUs," *CrystEngComm* 20 (2018): 5108–5111.

63. F. C. N. Firth, M. J. Cliffe, D. Vulpe, et al., "Engineering New Defective Phases of UiO Family Metal–organic Frameworks with Water," *Journal of Materials Chemistry A* 7 (2019): 7459–7469.

64. M. Ermer, J. Mehler, M. Kriesten, Y. S. Avadhut, P. S. Schulz, and M. Hartmann, "Synthesis of the Novel MOF hcp UiO-66 Employing Ionic Liquids as a Linker Precursor," *Dalton Transactions* 47 (2018): 14426–14430.

65. S. R. Teeparthi, E. W. Awin, and R. Kumar, "Dominating Role of Crystal Structure over Defect Chemistry in Black and White Zirconia on Visible Light Photocatalytic Activity," *Scientific Reports* 8 (2018): 5541.

66. A. L. Semrau and R. A. Fischer, "High-Quality Thin Films of UiO-66-NH_2 by Coordination Modulated Layer-by-Layer Liquid Phase Epitaxy," *Chemistry – A European Journal* 27 (2021): 8509–8516.

67. W. Morris, S. Wang, D. Cho, et al., "Role of Modulators in Controlling the Colloidal Stability and Polydispersity of the UiO-66 Metal–Organic Framework," *ACS Applied Materials & Interfaces* 9 (2017): 33413–33418.

68. S. Bakhshi, N. Zin, H. Ali, et al., "Simple and Versatile UV-Ozone Oxide for Silicon Solar Cell Applications," *Solar Energy Materials and Solar Cells* 185 (2018): 505–510.

69. N. Kumar, C. Maldarelli, C. Steiner, and A. Couzis, "Formation of Nanometer Domains of One Chemical Functionality in a Continuous Matrix of a Second Chemical Functionality by Sequential Adsorption of Silane Self-Assembled Monolayers," *Langmuir* 17 (2001): 7789–7797,

70. M. Treger, A. Hannebauer, A. Schaate, J. L. Budde, P. Behrens, and A. M. Schneider, "Tuning the Optical Properties of the Metal–organic Framework UiO-66 *via* Ligand Functionalization," *Physical Chemistry Chemical Physics* 25 (2023): 6333–6341.

71. M. Fukuto, R. K. Heilmann, P. S. Pershan, A. Badia, and R. B. Lennox, "Monolayer/Bilayer Transition in Langmuir Films of Derivatized Gold Nanoparticles at the Gas/Water Interface: An X-Ray Scattering Study," *The Journal of Chemical Physics* 120 (2004): 3446–3459.

72. A. V. Rogachev, N. N. Novikova, M. V. Kovalchuk, et al., "Permeation of Nanoparticles into Pulmonary Surfactant Monolayer: In Situ X-Ray Standing Wave Studies," *Langmuir* 38 (2022): 3630–3640.

73. C. Appel, B. Kuttich, L. Stühn, R. W. Stark, and B. Stühn, "Structural Properties and Magnetic Ordering in 2D Polymer Nanocomposites: Existence of Long Magnetic Dipolar Chains in Zero Field," *Langmuir* 35 (2019): 12180–12191.

74. J. E. Warias, F. Reise, S. C. Hövelmann, et al., "Photoinduced Bidirectional Switching in Lipid Membranes Containing Azobenzene Glycolipids," *Scientific Reports* 13 (2023): 11480.

75. O. O. Semivrazhskaya, D. Salionov, A. H. Clark, et al., "Deciphering the Mechanism of Crystallization of UiO-66 Metal-Organic Framework," *Small* 19 (2023): 2305771.

76. M. Taddei, J. A. van Bokhoven, and M. Ranocchiari, "Influence of Water in the Synthesis of the Zirconium-Based Metal–Organic Framework UiO-66: Isolation and Reactivity of $[ZrCl(OH)_2(DMF)_2]Cl$," *Inorganic Chemistry* 59 (2020): 7860–7868.

77. H. Xu, S. Sommer, N. L. N. Broge, J. Gao, and B. B. Iversen, "The Chemistry of Nucleation: In Situ Pair Distribution Function Analysis of Secondary Building Units During UiO-66 MOF Formation," *Chemistry – A European Journal* 25 (2019): 2051–2058.

78. D. Zhang, J. Hu, K. M. Kennedy, and I. P. Herman, "Forming Nanoparticle Monolayers at Liquid–Air Interfaces by Using Miscible Liquids," *Langmuir* 32 (2016): 8467–8472.

79. I. Peterson, "Langmuir-Blodgett Films," *Journal of Physics D: Applied Physics* 23 (1990): 379.

80. N. Tuccitto, T. Amato, C. M. A. Gangemi, et al., "Driving Coordination Polymer Monolayer Formation by Competitive Reactions at the Air/Water Interface," *Langmuir* 34 (2018): 11706–11713.

81. J. T. Culp, A. N. Morgan, M. W. Meisel, and D. R. Talham, "Metal Cyanide Networks Formed at an Air-Water Interface: Structure and Magnetic Properties," *Materials Research Society Online Proceedings Library* 658 (2000): 2.

82. Z. Wang, Y. Chu, G. Zhao, et al., "Study of Surface Wettability of Mineral Rock Particles by an Improved Washburn Method," *ACS Omega* 8 (2023): 15721–15729.

83. L. Celaya-Azcoaga, J. Pascual-Colino, G. Beobide, et al., "Chiral Supramolecular Proton Conductors: Harnessing Highly Charged Zirconium-Amino Acid Oxo-Clusters," *Inorganic Chemistry* 63 (2024): 23363–23373.

84. F. R. Kogler, M. Jupa, M. Puchberger, and U. Schubert, "Control of the Ratio of Functional and Non-Functional Ligands in Clusters of the Type $Zr_6O_4(OH)_4(carboxylate)_{12}$ for their Use as Building Blocks for Inorganic–organic Hybrid Polymers," *Journal of Materials Chemistry* 14 (2004): 3133–3138.

85. J. Pascual-Colino, B. Artetxe, G. Beobide, et al., "The Chemistry of Zirconium/Carboxylate Clustering Process: Acidic Conditions to Promote Carboxylate-Unsaturated Octahedral Hexamers and Pentanuclear Species," *Inorganic Chemistry* 61 (2022): 4842–4851.

86. Q. Sun, C. Liu, G. Zhang, J. Zhang, C.-H. Tung, and Y. Wang, "Aqueous Isolation of 17-Nuclear Zr/Hf Oxide Clusters during the Hydrothermal Synthesis of ZrO_2/HfO_2," *Chemistry – A European Journal* 24 (2018): 14701–14706.

87. F. Venel, C. Volkringer, O. Lafon, and F. Pourpoint, "Probing Adsorption of Water and DMF in UiO-66(Zr) Using Solid-State NMR," *Solid State Nuclear Magnetic Resonance* 120 (2022): 101797.

Supporting Information

Additional supporting information can be found online in the Supporting Information section. **Supporting Fig. S1:** PDF fit for synthesized **Hf12**-acetate and **Zr12**-acetate clusters in solid-state with their crystal structures. See Table S1 for refined parameters. **Supporting Fig. S2:** PDF fit for 10 mM aqueous solution of **Hf12**-acetate and **Zr12**-acetate clusters with their crystal structures. See Table S2 for refined parameters. **Supporting Fig. S3:** PDF fit for 10 mM aqueous solution of **Hf12**-acetate cluster with different structure models extracted from the crystal structures of zirconium analogs.[S13–S15] See Table S2 for refined parameters. **Supporting Fig. S4:** PDFs of a 10 mM aqueous **Hf12**–acetate solution measured immediately after dissolution and after 48 hours, fitted using the μ_2-oxo-bridged **Hf12**–formate structural model. Refined parameters are given in Table S3. **Supporting Fig. S5:** PDF for 10 mM aqueous solution of **Hf12**-acetate cluster with different concentrations of acetic acid, formic acid, or hydrochloric acid. The pH of the final solution and the goodness of fit (*Rw*) after fitting with **Hf12**-formate from **Hf36** structure model are also mentioned. See Table S4 for refined parameters. **Supporting Fig. S6:** BAM micrographs of a monolayer of **3** on a 10 µM **Hf12**-acetate aqueous solution (A–C), before compression (A), at the isotherm takeoff (B), and at a surface pressure of π=20 mN m^{-1} (C). Scale bar: 100 µm. **Supporting Fig. S7:** (A) Surface pressure-area compression isotherms of **2** on pure water and on aqueous solutions containing 10 µM of **Zr12** or **Hf12** acetate. BAM micrographs of a monolayer of **2** on pure water (B), on a 10 µM **Zr12**-acetate aqueous solution (C–E), and on a 10 µM **Hf12**-acetate aqueous solution (F–I), before compression (B, C, F), at the isotherm takeoff (D, G), and at a surface pressure of π=20 mN m^{-1} (E, I). Scale bar: 100 µm. **Supporting Fig. S8:** (A) Surface pressure-area compression isotherms of **4** on pure water and on aqueous solutions containing 10 µM of **Zr12** or **Hf12** acetate. BAM micrographs of a monolayer of **4** on pure water (B-D), on a 10 µM **Zr12**-acetate aqueous solution (E-G), and on a 10 µM **Hf12**-acetate aqueous solution (H-J), before compression (B, E, H), at the isotherm takeoff (C, F, I), and at a surface pressure of π=20 mN m^{-1} (D, G, J). Scale bar: 100 µm. **Supporting Fig. S9:** (A) Surface pressure-area compression isotherms of **5** on pure water and on aqueous solutions containing 10 µM of **Zr12**-acetate. BAM micrographs of a monolayer of **5** on pure water (B-D), and on a 10 µM **Zr12**-acetate aqueous solution (E-G), before compression (B, E), at the isotherm takeoff (C, F), and at a surface pressure of π=20 mN m^{-1} (D, G). Scale bar: 100 µm. **Supporting Fig. S10:** (A) Surface pressure-area compression isotherms of **6** on pure water and on aqueous solutions containing 10 µM-acetate. BAM micrographs of a monolayer of **6** on pure water (A), and on a 10 µM **Zr12**-acetate aqueous solution (C–E), before compression (B, C), at the isotherm takeoff (D), and at a surface pressure of π=20 mN m^{-1} (E). Scale bar: 100 µm. **Supporting Fig. S11:** (A) Surface pressure-area compression isotherms of **7** on pure water and on aqueous solutions containing 10 µM-acetate. BAM micrographs of a monolayer of **7** on pure water (B), and on a 10 µM **Zr12**-acetate aqueous solution (C–E), before compression (B, C), at the isotherm takeoff (D), and at a surface pressure of π=20 mN m^{-1} (E). Scale bar: 100 µm. **Supporting Fig. S12:** Parameters of a typical Langmuir isotherm. **Supporting Fig. S13:** Molecular areas (A), collapse pressure (B), slope (C) and static elastic modulus (D) of different amphiphiles (**2-7**) on a 10 µM **Zr12**-acetate aqueous solution. Static elastic modulus is defined as the negative of first derivative of the Langmuir isotherm. **Supporting Fig. S14:** Water-droplet based contact angle measurements on OTS-coated Si wafer before (A) and after (B) **3**-**Zr12** monolayer transfer. **Supporting Fig. S15:** Water-droplet based contact angle measurements on OTS-coated Si wafer before (A) and after (B) **3**-**Hf12** monolayer transfer. **Supporting Fig. S16:** X-ray photoelectron survey spectra of the monolayer of **3** prepared on **Zr12**-acetate, transferred on HOPG substrate. **Supporting Fig. S17:** O1s XPS of the monolayer of **3** prepared on **Zr12**-acetate, transferred on HOPG substrate. The O1s spectrum is deconvoluted into contributions corresponding to oxygen atoms in different chemical environments. **Supporting Fig. S18:** (A) Zr3d, (B) F1s, (C) O1s, and (D) C1s X-ray photoelectron spectra of the monolayer of **7** prepared on **Zr12**-acetate, transferred on HOPG substrate. The O1s and C1s spectra are deconvoluted into contributions corresponding to oxygen and carbon atoms in different chemical environments, respectively. **Supporting Fig. S19:** (A) Survey spectra, (B) Hf7f, (C) O1s, and (D) C1s X-ray photoelectron spectra of the monolayer of **3** prepared on **Hf12**-acetate, transferred on OTS-coated silicon wafer. The O1s and C1s spectra are deconvoluted into contributions corresponding to oxygen and carbon atoms in different chemical environments, respectively. **Supporting Fig. S20:** ToF-SIMS positive (yellow) and negative (blue) ion mode spectra of **3** on silicon wafer. **Supporting Fig. S21:** ToF-SIMS positive ion mode spectra of 3-Zr12 transferred on mica substrate, with UiO-66 provided as a reference. **Supporting Fig. S22:** (A) ToF-SIMS negative ion mode spectra of **3**-**Hf12** transferred on mica substrate. B and C show the spatial distribution of HfO_3H^- and the amphiphile **3** fragment, respectively. Scale bar = 100 µm; MC = maximum counts. **Supporting Fig. S23:** ToF-SIMS positive ion mode spectra of **3**-**Hf12** transferred on mica substrate. **Supporting Fig. S24:** HAADF STEM micrograph illustrating electron-beam-induced damage in the **3**–**Zr12** monolayer. The image was acquired at higher magnification (pixel size 91 pm, 1k × 1k resolution, 5 µs dwell time, <10 pA probe current) compared to damage-free imaging conditions. Despite the identical probe current, the increased electron dose density leads to structural decomposition of the monolayer. Beam-damaged regions are indicated by arrows. **Supporting Fig. S25:** Ellipsometric measurements of (A) bare silicon wafer with native silicon oxide layer, (B) octadecyltrichlorosilane (OTS) modified silicon wafer, and (C) monolayer of **3** prepared on **Zr12**-acetate, transferred on OTS-coated Si wafer. The thickness of layers is provided in Table S6 . **Supporting Fig. S26:** Ellipsometric measurements of **3**-**Hf12** monolayer, transferred on OTS-coated Si wafer. The thickness of layers is provided in Table S6. **Supporting Fig. S27:** (A) AFM micrograph of the **3**-**Hf12** monolayer transferred onto an HOPG. (B) Magnified view of a selected region. The overlaid lines in both images indicate the positions of the line profiles shown below, highlighting the height variations across the monolayer. **Supporting Fig. S28:** Schematic illustration of the different regions of the monolayer contributing to the overall scattering length density. **Supporting Fig. S29:** PDFs of 10 mM solution of **Hf12**-acetate cluster in DMF-water (80:20) mixture measured immediately after dissolution and after 48 hours, fitted with the μ_2-oxo-bridged **Hf12**–formate structural model. Refined parameters are given in Table S9. **Supporting Fig. S30:** Brewster angle micrograph of the air–pure DMF interface, taken at the Brewster angle (55°). Scale bar: 100 µm. **Supporting Fig. S31:** Water-droplet based contact angle measurements on OTS-coated Si wafer before (A) and after (B) **3**-**Zr12** monolayer transfer from the air–DMF interface. **Supporting Fig. S32:** (A) Survey, and (B) O1s X-ray photoelectron survey spectra of the monolayer of **3**-**Zr12** monolayer formed at the air-DMF interface, transferred on OTS-coated silicon wafer. In (C), no signals were detected in the 390–405 eV range, confirming the absence of N1s contributions and thus indicating that no residual DMF remains in the monolayer. **Supporting Fig. S33:** ToF-SIMS (A) positive and (B) negative ion mode spectra of **3**-**Zr12** multilayers formed at the air-DMF interface and transferred onto mica substrate. **Supporting Fig. S34:** Ellipsometric measurements of **3**-**Zr12** monolayer formed at the air-DMF interface, transferred onto OTS-coated silicon wafer. The thickness of layers is provided in Table S10. **Supporting Table S1:** Refined parameters for the PDF fit of synthesized **Hf12**-acetate and **Zr12**-acetate clusters in solid-state with their crystal structures, M = Hf/Zr. **Supporting Table S2:** Refined parameters for 10 mM aqueous solution of **Hf12**-acetate and **Zr12**-acetate clusters after fitting with different crystal structures. **Supporting Table S3:** Refined parameters for the PDF fit of 10 mM aqueous solution of **Hf12**-acetate cluster measured immediately after dissolution and after 48 hours, fitted using the μ_2-oxo-bridged **Hf12**–formate structural model. **Supporting Table S4:** Refined parameters for 10 mM aqueous solution of **Hf12**-acetate cluster with different concentrations of acetic acid, formic acid, or hydrochloric acid after fitting with **Hf12**-formate from **Hf36** structure model. **Supporting Table S5:** Parameters obtained from Langmuir isotherms for different amphiphiles on **Zr12**/**Hf12**-acetate solutions. Area (A) values are expressed in $Å^2$/molecule. **Supporting Table S6:** Thickness of the layers obtained from ellipsometry. **Supporting Table S7:**

Calculated and experimental scattering length densities of individual components of the **3**-**Zr12** monolayer. **Supporting Table S8:** Parameters determined by fitting the X-ray reflectivity curve. **Supporting Table S9:** Refined parameters for the PDF fit of 10 mM solution of **Hf12**-acetate cluster in DMF-water (80:20) mixture measured immediately after dissolution and after 48 hours, fitted using the μ_2-oxo-bridged **Hf12**–formate structural model. **Supporting Table S10:** Thickness of the layers obtained from ellipsometry.